This is the preprint of the contribution published as:

Zhang, B., Zheng, T., Zheng, X., Jiang, S., Cao, M., **Walther, M.**, Lu, C. (2023):
Dynamics of upstream saltwater intrusion driven by tidal river in coastal aquifers
Sci. Total Environ. **877** , art. 162857

The publisher's version is available at:

http://dx.doi.org/10.1016/j.scitotenv.2023.162857

Dynamics of upstream saltwater intrusion driven by tidal river in coastal aquifers

Bo Zhang[1,3], Tianyuan Zheng[1,2*] Xilai Zheng[1,2], Shiqiang Jiang[4], Min Cao[4], Marc Walther[5], Chunhui Lu[6]

1. College of Environmental Science and Engineering, Ocean University of China, Qingdao 266100, China

2. Key Laboratory of Marine Environment and Ecological Education, Ocean University of China, Qingdao 266100, China

3. College of Marine Geosciences, Ocean University of China, Qingdao 266100, China

4. Qingdao Hydrological Center, Qingdao 266101, Shandong, China

5. Helmholtz-Centre for Environmental Research–UFZ Leipzig, Department of Environmental Informatics, 04318 Leipzig, Germany

6. State Key Laboratory of Hydrology-Water Resources and Hydraulic Engineering, Hohai University, Nanjing, China

*Corresponding author:

Tianyuan Zheng (zhengtianyuan@ouc.edu.cn)

College of Environmental Science and Engineering, Ocean University of China, Qingdao 266100, China.

Abstract

Recent research has shown that the tidal river has a significant effect on saltwater intrusion (*SWI*) in coastal aquifers, but it is currently unclear how the tidal river contributes to the upstream groundwater flow and salinity distribution. This study examined the effects of a tidal river on the dynamic characteristics of groundwater flow and salt transport in a river-coastal aquifer system using field monitoring data and numerical simulations. It was found that changes in tidal-river level led to the reversal of groundwater flow, and the *SWI* area in the aquifer varied over time, particularly for the low-concentration saltwater area (for the area between 250 mg/L and 500 mg/L of Cl^-) and the medium-concentration saltwater area (for the area between 500 mg/L and 1000 mg/L of Cl^-). Results indicated that tidal river forces caused a 5% change in the *SWI* region during a tide cycle which implies tidal-river-induced *SWI* at distinct tidal stages is significantly different. In addition, we quantified the water exchange and salt flux between the tidal river and aquifer and found that under tidal conditions, the water and salt fluxes across the aquifer-river interface typically varied considerably over time. The presence of a physical river dam can amplify the difference in water level between high and low tides, thereby enhancing the influence of a tidal river on water exchange and salt flux. The findings lay the foundation for gaining a comprehensive understanding of the tidal river on groundwater flow and salt transport in upstream aquifers.

Keywords: Tidal river; Coastal aquifer; Saltwater intrusion; Water exchange; Numerical models

1 Introduction

The density of coastal populations is increasing rapidly throughout the world (Sherif et al., 2012; Sefelnasr and Sherif, 2014; Lu et al., 2017; Shi et al., 2020). Additionally, groundwater resources are overused for agricultural and industrial purposes (Walther et al., 2012; Lu and Werner, 2013; Zhang et al., 2020; Zheng et al., 2020). Due to the general rise in sea level caused by climate change, substantial quantities of saltwater infiltrate coastal aquifers, causing severe groundwater degradation. Consequently, saltwater intrusion (*SWI*) has become a worldwide concern (Werner et al., 2013; Lu et al., 2015; Tully et al., 2019; Fang et al., 2021).

SWI is significantly influenced by a number of factors, including the density (Shen et al., 2015), recharge variability (Xin et al., 2010), anthropogenic influences (Xiao et al., 2018; Zheng et al., 2020), aquifer hydraulic (Gardner, 2007), and tides (Wilson and Gardner, 2006; Moffett et al., 2010; Wilson and Morris, 2012). In recent years, greater emphasis has been placed on comprehending the effects of tides on *SWI*. According to Ataie-Ashtiani et al. (1999), Robinson et al. (2006), and Werner et al. (2013), tides are a global phenomenon that affects the salinity distributions in coastal aquifers. Tidal fluctuations can create a thick mixing zone (Yu et al., 2019) and limit the landward and seaward movement of the saltwater wedge (Kuan et al., 2019). Additionally, an upper saline plume (USP) forms in the intertidal zone due to the tide-induced circulation of saltwater (Kuan et al., 2012). The USP transitions from stable to unstable states due to tidal and inland freshwater inputs (Fang et al., 2021). However, the *SWI* scenarios discussed in previous studies were limited to projections parallel to the coast, and the influence of tidal rivers with more complex geometries was disregarded.

Recent attention has been drawn to the effects of tidal rivers on coastal aquifers. Using two-dimensional numerical modeling for a lateral cross-section, Werner and Lockington (2006) studied the behavior of groundwater flow and salinity in a phreatic aquifer adjacent to a permeating tidal estuary. They demonstrated that tidal fluctuations in estuaries can significantly affect the salinity distribution in adjacent density-stratified phreatic aquifers. Lenkopane et al. (2009) conducted a series of numerical simulations and discovered that tidal salinity fluctuations (synchronous with the estuary stage) can affect the magnitude and distribution of groundwater discharge to the estuary. Xiao et al. (2019) discovered that tides significantly enhance the exchange of surface water and ground water. All previous research assumed that simulated aquifers were directly connected to the coastline, thereby attributing the tidal effects to the seaside boundary. However, it has been demonstrated that the effect of tide-induced changes in the water level and salinity of rivers on the hydrological system can occur far from the coast (tens of kilometers).

Tidal river dynamics is governed primarily by the interactions between tides, river flows, and coastal currents, which are influenced by climate change and human activity (Xue et al., 2009; Wang et al., 2019). Long-distance *SWI* is prevalent, especially in semi-arid regions (Jeong et al., 2010). Muchamad et al. (2020) numerically simulated saltwater pollution in a river in Indonesia's Cimanuk River Estuary following dam failure. They discovered that the river's maximum salinity reached 90 kilometers upstream. Utilizing numerical modeling (Cheng et al., 2012; Zahed et al., 2008; Zou and Li, 2010), field observations (Gong and Shen, 2011), and analytical studies (Cai et al., 2015; Prandle, 2004; Zhang et al., 2011), researchers have investigated tide-induced river pollution. However, the effects of tidal rivers on subsurface *SWI* in the upstream are still unknown.

This study examines the effects of tidal rivers on *SWI* in aquifers not directly connected to the coast. The primary objectives of this study were to (1) investigate the dynamic changes in the groundwater flow field in a real coastal aquifer affected by a tidal river, (2) investigate the effects of a tidal river on the spatiotemporal distribution characteristics of *SWI*, and (3) quantify the effect of tides on the water exchange and salt flux between the river and aquifer.

2 Study area

2.1 Location and Climate

The study area is located in Qingdao, China, downstream of the Dagu

River near Jiaozhou Bay, covering an area of ~42 km^2 (Fig. 1). The study area is located ~10 km from the coastline.

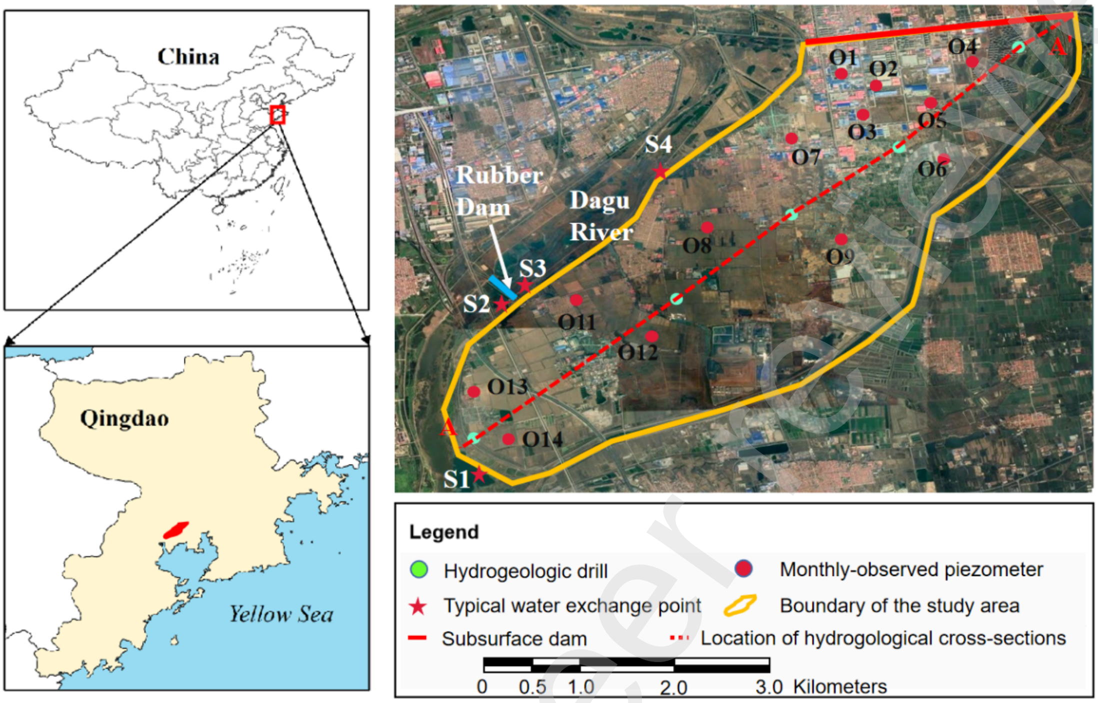

Fig. 1 Location of the study area.

Monthly precipitation, evaporation (measured by an evaporating pan), and air temperature during 2011–2020 are 678 mm, 1044 mm, and 12.5 °C, respectively (Fig. 2).

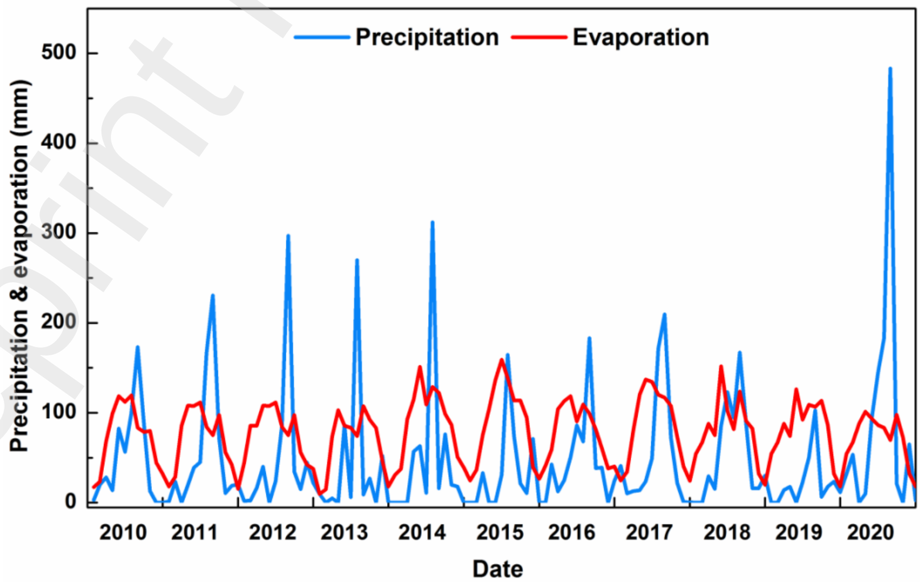

Fig. 2 Monthly precipitation and evaporation from January 2011 to December 2020.

2.2 Hydrology

The Dagu River is located west of the area of study and empties into Jiaozhou Bay. A 400-meter-long, 3.5-meter-tall inflatable tidal dam was constructed on the Dagu River to block the tides' upstream movement.

Fig. 3 depicts a time series of the observed tidal and river levels at various locations (S1-S4 in Fig. 1) The tidal pattern is semi-diurnal, with one cycle lasting 12 hours. The four phases of a tidal cycle were (a) high tide, (b) falling mid-tide, (c) low tide, and (d) rising mid-tide. During the period of observation, the highest and lowest tide levels were 4.89 and 0.12 meters above sea level (asl), respectively.

It indicated that the study area has a significant tide range. When the tide was lower than the riverbed, the dam prevented any water from flowing upstream, and there was no water downstream. Thus, the river water level monitoring data at locations S1 and S2 were discontinuous. As in S1 and S2, the low and high river levels followed the low and high tide levels. The lag between river level fluctuations at S2 and S1 was longer than at S1. Throughout the observation period, the river levels of S3 and S4 remained constant at 2,6 m. This was primarily due to the tidal dam between S2 and S3, which prevented saltwater from flowing.

In addition, river water samples were collected to determine the Cl^- concentration, which was estimated to be 22000 mg/L. The Cl^- concentrations of S3 and S4 were significantly lower than those of S1 and S2, with S3 (320 mg/L) having a higher concentration than S4 (110 mg/L).

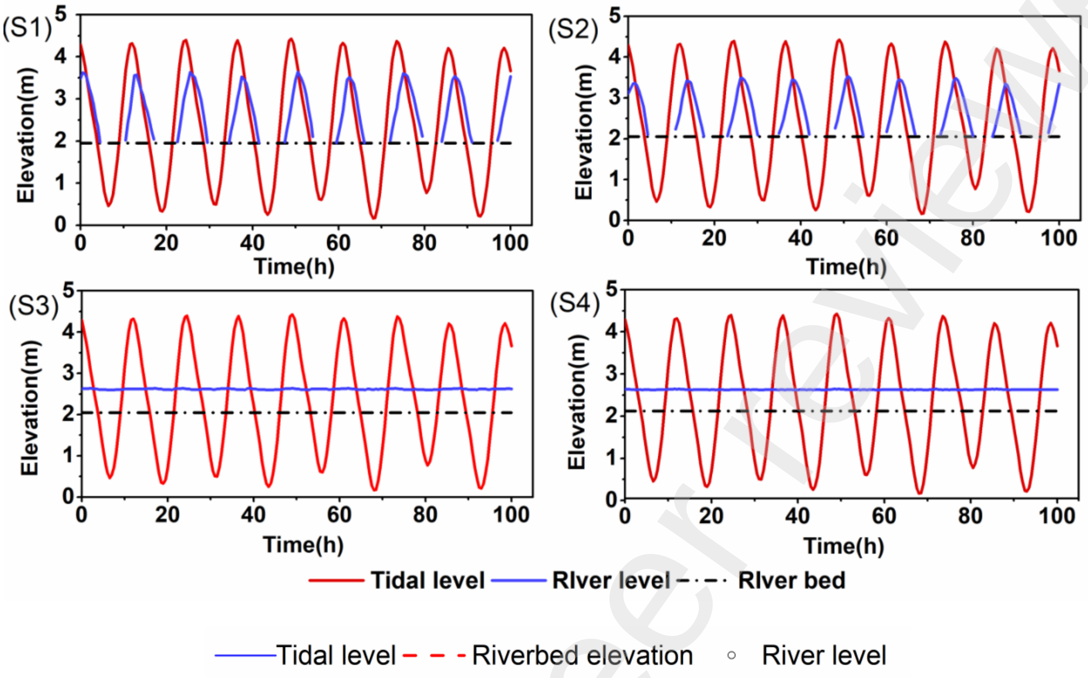

Fig. 3 Observed tidal and river levels at the four typical points in the study area. S1 is the southernmost in the study area and the closest position to the sea. S2 and S3 are the outside and inside position of the tide dam. S4 is the most inland of the four points and is located 3 km north of the tidal dam.

2.3 Hydrogeology

The aquifer in the study area is two-layered and unconfined. The upper layer is 0.5–12 m thick and composed of clay and sandy clay. The lower layer is 4.0–16.6 m thick and composed of medium to fine sand are the main components of the lower layer. A sediment layer lies between the river and the aquifer with a hydraulic conductivity of 0.06 – 0.38 m/d (Zhang et al., 2021).

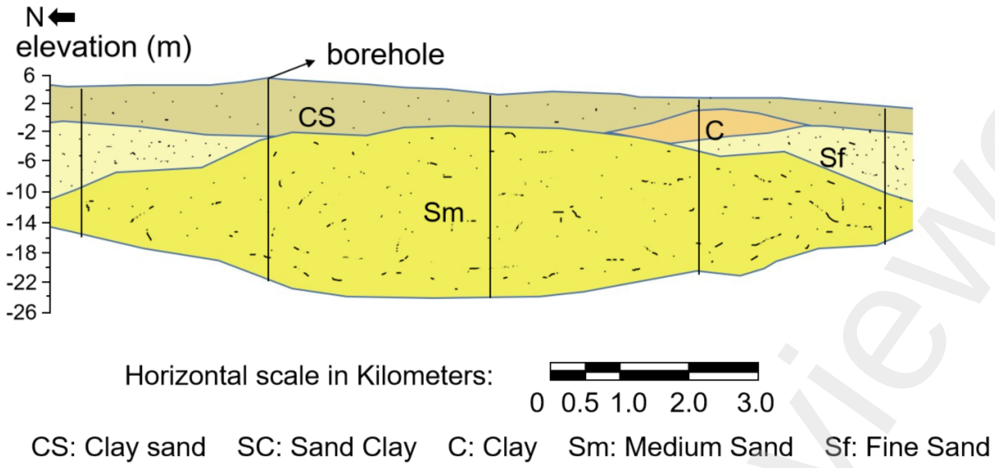

Fig. 4 Hydrogeological cross-section of the study area (red dotted line in Fig. 1).

Groundwater in the study area flows from north to south. A 4.2 km-long subsurface dam was constructed at the northern boundary of the study area in 1998 to prevent *SWI*, cutting off the hydraulic connection between the study area and the upstream regions.Monthly groundwater samples were collected between 2019 and 2020 from 14 observation wells at depths of 4–6 m.

3 Model setup

3.1 Conceptual model

Consideration was given to the mechanisms of groundwater flow and salt transport under the influence of tidal rivers. To simplify the problems, the following assumptions were made: (1) the aquifer was divided into two layers based on its lithology; (2) the varying total stress on the riverbed due to variations in water depth during submersion was disregarded; and (3) the Cl^- concentration of the river water was uniform vertically.

The model's boundary conditions were defined as follows: (1) the northern boundary of the study area (cutoff wall) and the aquifer base were defined as a no-flow boundary; (2) the top boundary was defined as recharge (from monitoring precipitation); (3) the remaining boundaries of the study area were the river boundaries; and (4) the river boundary was assigned as a specified head and concentration (Cl^-) boundary, with values taken from field monitoring.

3.2 Numerical model

MODFLOW-2000 and MT3DMS were employed to simulate the groundwater flow and solute transport (El-Zehairy et al., 2018). In addition, we used the SFR2-based coupled model quantify the interactions between surface water and groundwater in the modeled tide-driven salt aquifer.

Standard density flow and transport equations in porous media were used for groundwater modeling (Guo and Langevin, 2002). The following methodology was used to describe the surface water components. The intersections of the river water levels varied temporally owing to the tide. Consequently, boundary conditions of the groundwater model at the intersection surface also varied temporally. For each node at the interface, (1) if the node was dry as per SFR2 (water depth less than a preset threshold value) with a negative pore water pressure (calculated from MODFLOW at the previous time step), it was defined as a no-flow boundary; (2) if the node was dry as per SFR2 with a positive pore water pressure, it was defined as part of a seepage face and specified by the atmospheric (zero) pressure (Wilson and Gardner, 2006); and (3) if the node was wet (inundated) as per SFR2, it was defined as a specified head boundary subject to hydrostatic pressure given by the local water depth.

The river was modeled using the SFR2 package of MODFLOW through Eq. (1):

$$Q_L = \frac{KwL}{m}(h_s - h_a) \tag{1}$$

where Q_L is the volumetric flow between a given section of the river and volume of the aquifer (m^3/d), K is the hydraulic conductivity of riverbed sediments (m/d), w is the representative width of the river (m), L is the length of the river corresponding to a volume of the aquifer (m), m is the thickness of the riverbed deposits (m), h_s is the stream-head determined by adding the river depth to the riverbed elevation (m), and h_a is the aquifer head (m).

The solute concentration in the river can be expressed using mass balance as in Eq. (2):

$$\sum Q_i(\Delta t)C_i - \sum Q_o(\Delta t)C_o = V_1^n C_1^n - V_1^{n-1}C_1^{n-1} \tag{2}$$

where Q_i and Q_o are the river inflow and outflow rates [m^3/d], respectively, C_i and C_o indicate the solute concentration of the river inflow and outflow [mg/L], respectively, V_1^n and V_1^{n-1} represent the volume of the river at the beginning of the current and previous time steps [m^3], respectively, and C_1^n and C_1^{n-1} are the solute concentrations in the river at the beginning of the current and previous time steps [mg/L], respectively.

The plane grid size was 50 × 50 m and two grids were used to represent a two-layered structure in the vertical direction (Zhang, 2021). Additionally, the aquifer also showed obvious lithological partitioning. The upper aquifer layer is mainly composed of clayey sand and sandy clay. Hydraulic conductivity (K_h) of the upper layer was estimated from on-site pumping tests to be 0.46–5 m/d. The lower aquifer layer is mainly composed of fine to medium sand have a K_h of 25.2–106.7 m/d. The measured longitudinal dispersivity (α_L) was set as 0.30–1.68 m. The specific yield (S_y) was set between 0.03 and 0.18 (Zeng et al., 2018). For river modeling, the Manning roughness coefficient was set to 0.015.

Precipitation infiltration parameters (α) and monthly precipitation were used to calculate the groundwater recharge rate. River evaporation was measured using an evaporating pan (100 mm diameter). Land surface evaporation was calculated using the limit evaporation depth, surface elevation, and maximum evaporation rate (Zhang et al., 2020). Initial groundwater levels and Cl^- concentrations in the study area were determined using monitoring data.

3.3 Model calibration

The results of model calibration are provided in Fig. 5, which show a good agreement between the simulated and measured groundwater levels, with a correlation coefficient of 0.97.

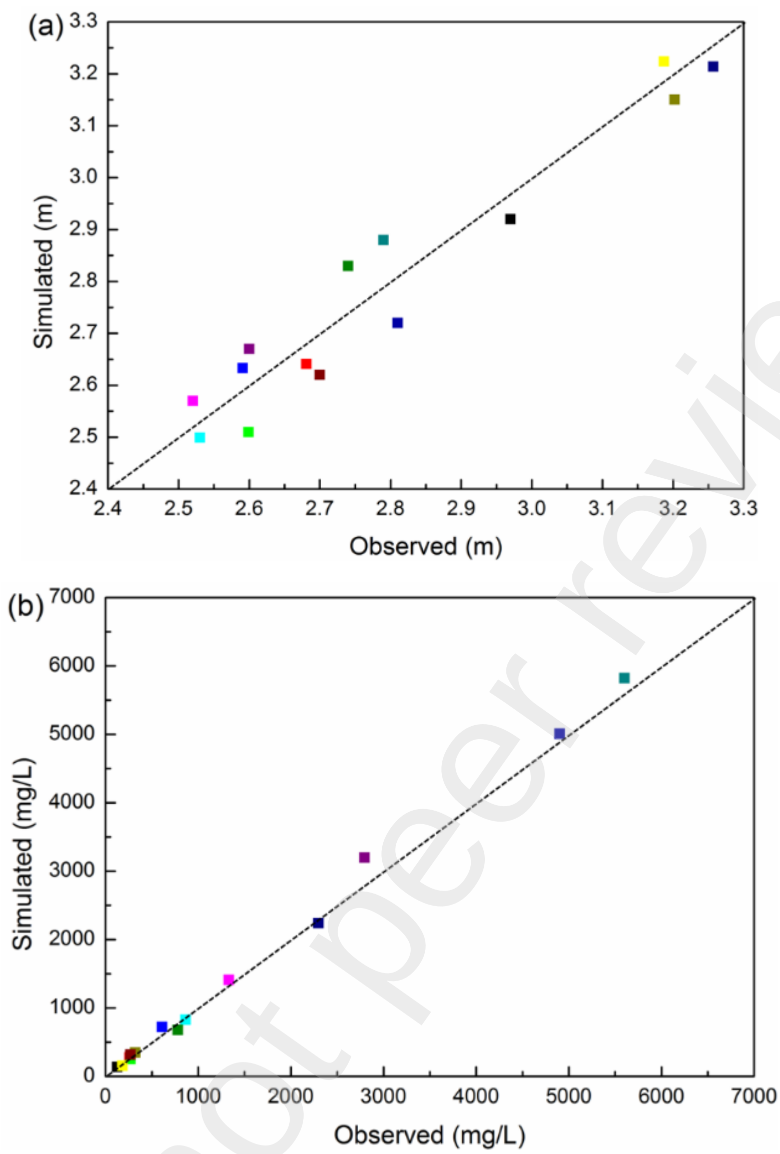

Fig. 5 Simulated vs. observed results of (a) groundwater level and (b) Cl^- concentration

The parameters of the reference case according to the model calibration are summarized in Table 1.

Table 1. Model parameters.

Parameters	Values	Units
Porosity *n*	0.40	[-]
Clay sand hydraulic conductivity	3.85	[m/d]
Sand clay hydraulic conductivity	0.89	[m/d]

Fine sand hydraulic conductivity	37.94	[m/d]
Medium sand hydraulic conductivity	89.25	[m/d]
Longitudinal dispersivity (α_L)	1.38	[m]
Transverse dispersivity (α_T)	$0.10\alpha_L$	[m]
Diffusion coefficient (D_0)	1.00	[10^{-6} m^2/d]
Clay sand specific yield (S_y)	0.08	[-]
Sand clay specific yield (S_y)	0.04	[-]
Fine sand specific yield (S_y)	0.15	[-]
Medium sand specific yield (S_y)	0.18	[-]
Precipitation infiltration parameters (α)	0.26	[-]
Manning coefficient	0.15	[-]

4 Result and discussion

4.1 Dynamic characteristics of groundwater and salt

4.1.1 Groundwater flow

The various states of tidal influence on coastal groundwater are depicted in Figure 6. Following the methodology of Xin et al. (2010), we illustrated transient groundwater flow fields based on groundwater flow direction (GFD) and velocity at the four typical tidal stages.

At high tide, the tidal river was filled with saltwater in Figure 6 (a). At this point, we may discover that the groundwater level downstream has risen higher than the groundwater level upstream. In the middle and downstream of the study area, a GFD reversal was observed. It was primarily due to the fact that the surface saltwater level was higher than the groundwater level and continued to penetrate the aquifer from the downstream due to the tidal dam, which prevented saltwater from flowing upward. Consistent with the findings of Xiao et al. (2019), who focused on the vertical bank of the estuary, the outcomes were as expected (rather than the tidally driven river aquifer studied here).

For the falling mid-tide stage (Figure 6(b)), the downstream groundwater level decreased substantially. Compared to the high tide level, the countercurrent area of groundwater has obviously decreased downstream. primarily due to a decrease in the river's lateral infiltration during the falling tide This is a typical infiltration pattern for an estuary aquifer (Lenkopane et al., 2009). At low tide, the counter current area of groundwater has disappeared. Because the dam prevented fresh water from entering the upstream river, the tide river was nearly dry. At this time, groundwater was released into the river below the dam. During the rising mid-tide stage, GFD reversal occurred once more in the southern portion of the study area (Figure 6(d)). Consequently, it can be inferred that the groundwater flow varied with the tide, especially in the vicinity of the tidal river. During the rising tide, surface water infiltration occurred, while groundwater discharge occurred during the falling tide (Li et al., 2008; Xin et al., 2011; Xiao et al., 2019). Notably, this phenomenon was more pronounced downstream of the rubber dam, suggesting that the rubber dam amplified the influence of tides on the groundwater flow field.

Furthermore, the GFD in the southwest changed completely within 12 hours, which can be explained by the following: 1) upstream aquifers in the coastal zone are relatively thick compared to those near the coast, which enhances the tidal effect on groundwater; 2) the riverbed sediments are less than those in the shoreline aquifers, and the exchange rate between saltwater and aquifer in the channel is obviously higher than that in the coastline; and 3) the presence of the tides, which accentuates the groundwater flow field variations between high and low tides.

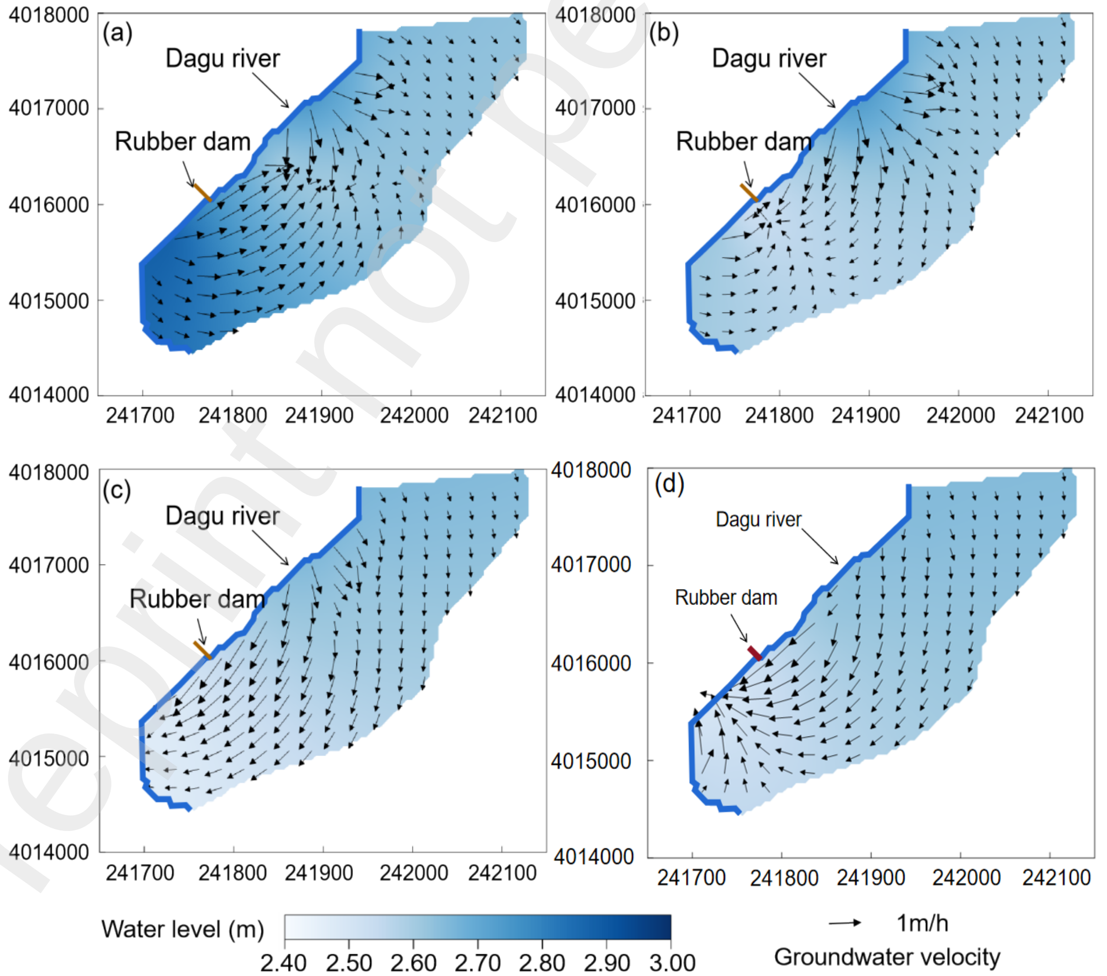

Fig. 6 Flow field at four typical tide stages: (a) high tide, (b) falling mid-tide, (c) low tide, and (d) rising mid-tide. The X-Y axis is the universal horizontal Mercator projection coordinate system, and its unit is meters. The short brown lines represent the rubber dam, which prevent the tide from moving further alone the river. The magnitude and direction of the Darcy velocity are reported as the length and direction of the arrow.

4.1.2 Salt distribution

Fig. 7 depicts the distribution of Cl^- concentration in groundwater at various tidal stages. Due to the constant recharging of the aquifer by freshwater, a small amount of freshwater was present northwest of the study area near the river at high tide (Fig. 7(a)). The Cl^- concentration in other regions was greater than 250 mg/L and increased gradually from north to south, reaching a maximum near the southern border and the river (>6,000 mg/L). In addition, the Cl^- concentration in the aquifer near the rubber dam was greater than 250 mg/L, and salty groundwater was discharged into the river upstream of the rubber dam. A river water sample collected north of the rubber dam revealed a Cl^- concentration of 280 mg/L, confirming this observation. This indicated that the saltwater intercepted by the rubber dam can bypass it via the aquifer and contaminate the river upstream of the rubber dam. In addition, we estimated a local maximum of Cl^- at the location where the water flow reversed direction. This further suggests that highly saline water flows upstream due to the influence of tides.

Under a falling tide, the groundwater area continued to expand far from the river (Fig. 7(b) and (c)), while the local maximum concentration of Cl^- in the saltwater decreased (Fig. This is due to the combined effects of increased groundwater recharge and decreased saltwater infiltration. The area of groundwater decreased once more as the tide rose (Figure 7(d)). Therefore, we conclude that the *SWI* range in the study area fluctuates periodically due to the influence of the tides.

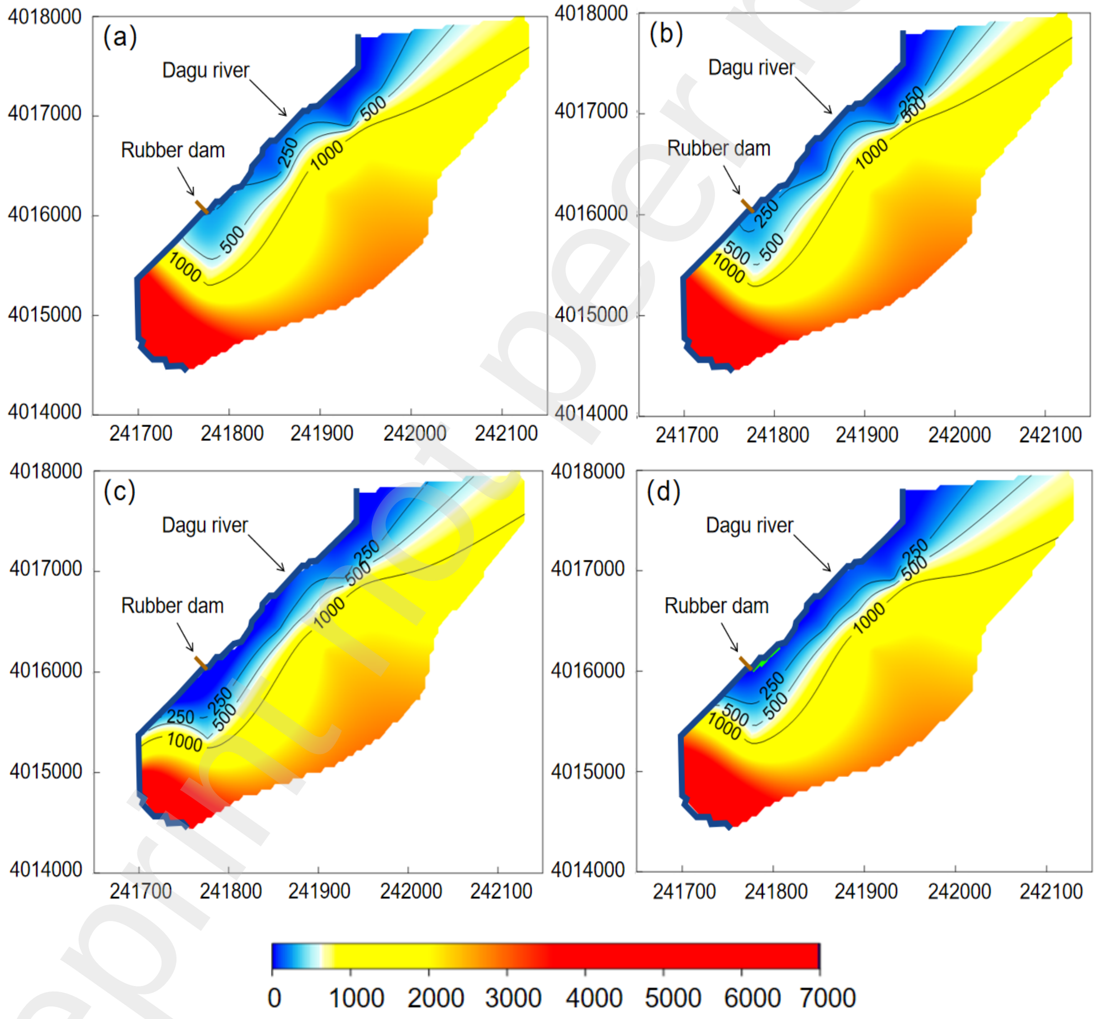

Fig. 7 Contour plots of Cl^- concentration in groundwater at four tidal stages: (a) high tide, (b) falling mid-tide, (c) low tide and, (d) rising mid-tide. The X-Y axis is the universal horizontal Mercator projection coordinate system, and its unit is meters. The short brown

lines represent the rubber dam, which prevent the tide from moving further alone the river. The blue area represent the fresh groundwater. The black thick solid line is the contour line of 250mg/L Cl^- concentration in groundwater which represent the boundary between salt and fresh groundwater.

To further describe the dynamics of the contaminated area, saltwater can be categorized as low-concentration saltwater (*LSW*, 250 mg/L ≤ Cl^- < 500 mg/L), medium-concentration saltwater (*MSW*, 500 mg/L ≤ Cl^- < 1000 mg/L), and high-concentration saltwater (*HSW*, 1000 mg/L ≤ Cl^-) (Zhang et al., 2021). The total saltwater (*TSW*), *LSW*, *MSW*, and *HSW* at different tidal stages are shown in Fig. 8.

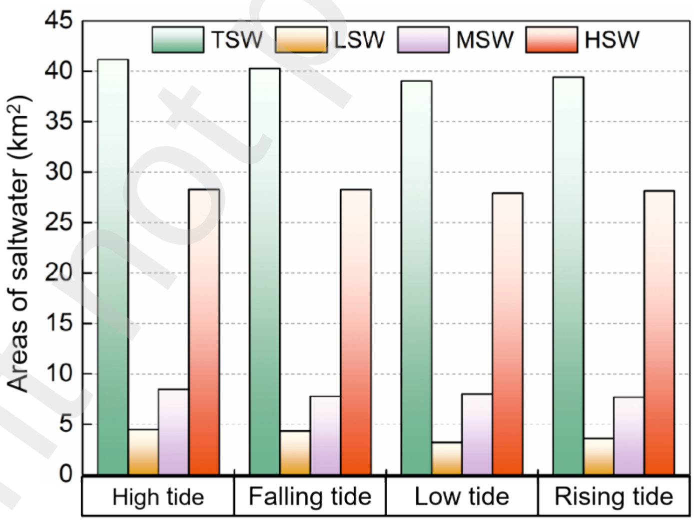

Fig. 8 Saltwater areas for high tide, falling mid-tide, low tide, and rising mid-tide stages. The blue column represent the total area of saltwater, the green column represent the area of low Cl^- concentration saltwater (250 mg/L≤ Cl^- < 500 mg/L), the yellow column represent the area of medium Cl^- concentration saltwater (500 mg/L≤ Cl^- < 1000 mg/L), the red column represent the area of high Cl^- concentration saltwater (1000 mg/L≤ Cl^-).

The *HSW*, *MSW*, *LSW*, and *TSW* areas were 4.44, 8.45, 28.27, and 41.16 km^2 at the high tide stage (Fig. 8). The *TSW* area decreased by 0.88 km^2 with the drop in tide level at the falling mid-tide stage. Notably, the *LSW* and *MSW* area were reduced by 0.15 and 0.71 km^2, respectively, while the *HSW* area was only reduced by 0.02 km^2. This shows that the salinity distribution of *LSW* and *MSW* at the high tide stage was more susceptible to the tidal influence.

The *TSW* decreased to 39.02 km^2 during the low-tide stage. The *HSW*, *MSW*, and *LSW* areas were 27.89, 7.80 and 3.33 km^2, respectively. The *TSW* area further decreased during this stage compared to the falling mid-tide stage. It was observed that river water level and freshwater recharge from upstream of the rubber dam decreases under tidal influence, while the *HSW* near the tidal river turns into *MSW* during the low tide stage (Fig. 7(c)). This suggests that tidal influence is significant at the low tide stage. The *TSW* area increased again during the rising tide stage and the *MSW* and *LSW* areas increased by 0.37 km^2 and 0.48 km^2, respectively, which is significantly more than for *HSW.* This is mainly because the *LSW* and *MSW* areas are near the river and more susceptible to changes in the water level and salinity from the tidal river. This also indicated that the tide-induced periodic changes in the saltwater and freshwater ranges mainly occur near the river.

4.2 Surface water and groundwater interactions

This study reveals the spatiotemporal characteristics of groundwater flow in the system of tidal river-aquifers. Through numerical modeling, the surface water and groundwater exchange is quantified in this section.

4.2.1 Water exchange

At various times during the tidal period, the water exchange rate per unit width between the aquifer and the river was calculated (Fig. 9), with positive values indicating that the river recharged the groundwater.

Figure 9 (a) depicts the water exchange at the location in the study area closest to the ocean (S1). Due to the tide, the water exchange rate variations were largely symmetrical. River water entered the aquifer at high and low tide (0 – 3 h and 9 – 12 h). During the remaining tidal period (3 – 9 h), groundwater discharged into the river at a maximum rate of -1.62 m/h when the tide level fell to 2.02 m above sea level. In the next three hours, the tidal level fluctuated by more than 1.5 m, but the groundwater discharge rate stabilized at -1.6 m/h because the tidal water level was lower than the riverbed elevation (2 m) and the river was dry at the time. The hydraulic gradient between the aquifer and the river remained constant, and the groundwater discharge rate reached its maximum.

Similarities were observed between the S1 and the position outside the tide dam in terms of water exchange (S2). The exchange rate could rise or fall with the tide and was symmetric over a tide cycle. Nonetheless, a significant difference was observed in this water exchange, with S2's exchange rate variations clearly lagging behind those of S1. At the falling mid-tide stage (the blue circle in Fig. 9(a) and (b)), for instance, the exchange rate of S1 ranged from 0.15 to -0.52 m/h, whereas the exchange rate of S2 remained constant at 1.1 m/h. The same phenomenon also occurred during the rising mid-tide stage (red circle in Figures 9(a) and (b)). The hysteretic change in the exchange rate is a result of the longer response time of the upper river reaches to tides.

The characteristics of water exchange differed between the downstream and upstream regions of the dam (Figure 9(c)). In the upper reaches of the rubber dam, the aquifer drained into the river at high tide and was recharged by the river at low tide. This observation was completely reversed after the dam was constructed. The primary cause is the stable river level upstream of the rubber dam, which is approximately 2.6 meters. This may cause the groundwater level to exceed the river at high tide. At 3 km upstream of the rubber dam, the exchange relationship between the river and the aquifer was distinct from the previous three locations (Fig. 9(d)). The river water continued to recharge the groundwater during the tidal period, and the recharge rate remained stable at 1.7 m/h primarily because: (1) tidal forces have little effect on the groundwater level far upstream of the rubber dam; and (2) the river water level remained stable and was higher than the groundwater level. The results demonstrated that the rubber dam diminished the effect of tidal forces on water exchange upstream of the dam.

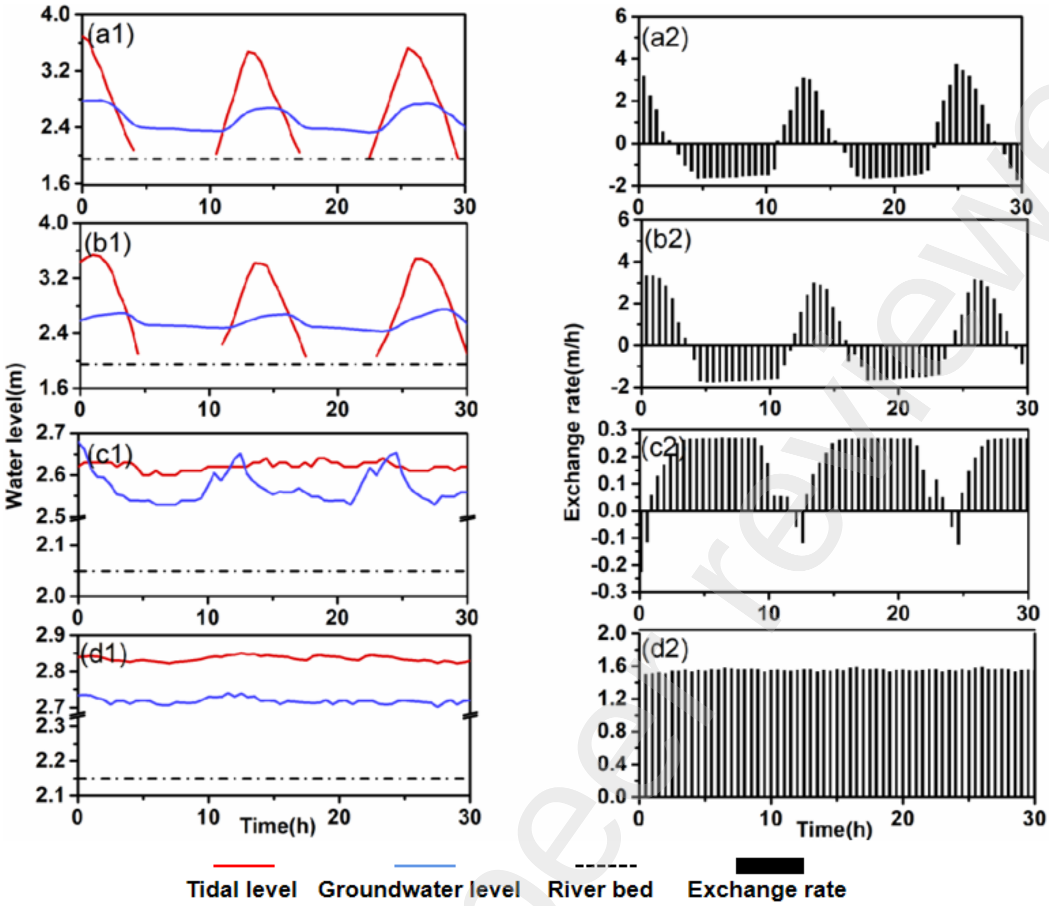

Fig. 9 Observed river and groundwater levels and simulated water exchange rate between river and groundwater at (a) the position closest to the sea in the study area, (b) the position outside of the tide dam, (c) the position inside of the tide dam, and (d) 3 km north of the tidal dam (most inland of the four points). Positive values represent groundwater recharge by the river and negative values represent groundwater discharge to the river. In (a) and (b), the red dotted line discontinuities indicated that there is no water in the river due to the influence of rubber dam and tide.

4.2.2 Salt flux

Water in the tidal river is the sea water driven by the tide. Therefore, the river and the aquifer experienced both water exchange and salt flux. Figure 10 compared the total net salt exchange (*TNSE*) per unit length between the aquifer and the different locations in the river. Positive values indicated that the groundwater receives salinity from the river.

Fig. 10 (a) represent the characteristics of the *TNSE* between the aquifer and downstream of the rubber dam. The figure showed that *TNSE* also changes regularly with changes in the tide level. In a tidal period, the maximum value of *TNSE* always appeared in the falling mid-tide stage. This can be attributed to the aforementioned finding that the water exchange relationship between the tidal river and aquifer reversed at the falling mid-tide. At the same time, the amount of groundwater recharged from the river reached its maximum. Moreover, compared to the next tidal periods, the maximum *TNSE* was observably reduced. This was mainly related to the weakening of tidal force. In addition, we could also find that the maximum *TNSE* of S1 was always higher than that of S2. The primary reason was that sea water decreased in salinity as it traveled along the river. This conclusion is consistent with the results from Xiao et al. (2019).

Fig 10 (b) shows an diferent *TNSE* trend compared to the Fig. 10 (a). This is because upstream of the rubber dam receives significantly less saline groundwater (Cl^- was ~300 mg/L) at high tide stage. Additionally, we observed that the *TNSE* at ~3 km upstream of the rubber dam was consistently positive at the end of the tidal period, leading to the the aquifer salinity constantly increasing. However, the *TNSE* downstream of the rubber dam was ~20 times higher than that upstream, indicating that building rubber dams in the river can prevent *SWI*.

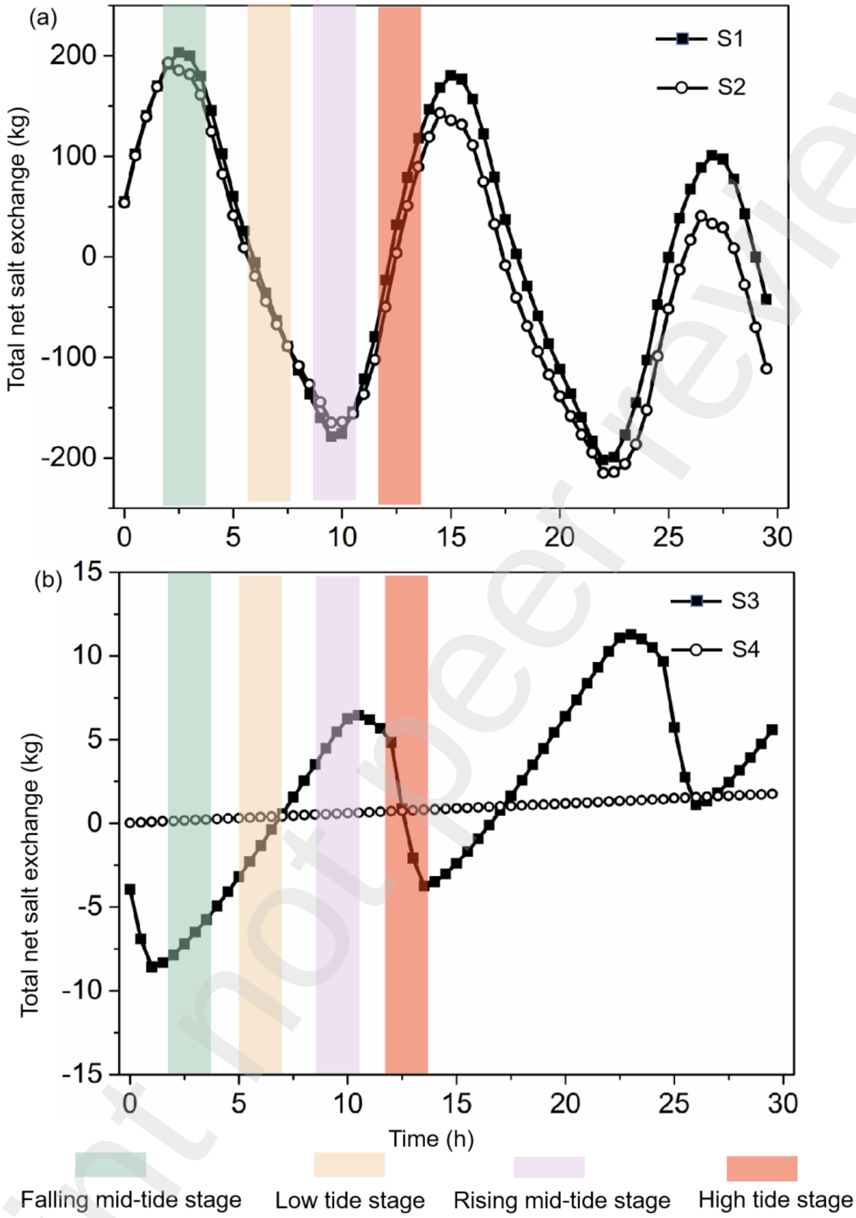

Fig. 10 Total net salt flux between surface water and groundwater at the four typical points in the study area. S1 is the southernmost in the study area and the closest position to the sea. S2 and S3 are the outside and inside position of the tide dam. S4 is the most inland of the four points and is located 3 km north of the tidal dam.

5 Summary and Conclusions

We presented field observations of tide-induced variations in the water levels of the Dagu River, as well as groundwater levels of the surrounding aquifer, and conducted a series of numerical simulations to quantify the influence of tidal dynamics of rivers on *SWI* in coastal aquifers.

The results demonstrated that during the rising-tide phase, the tidal river level rises rapidly above the aquifer's groundwater table. A substantial amount of surface saltwater infiltrated the aquifer via the tidal river-aquifer interface. Meanwhile, the direction of groundwater flow downstream was reversed. In addition, the tidal dam blocked the tide and increased the influence of the tidal river on the groundwater. At the high tide stage, the influence of the tidal river on groundwater was greater than at the rising tide stage. During the falling-tide stage, the river level will rapidly fall below the groundwater table until there is no water in the river. In the meantime, the groundwater downstream of the tidal dam will also discharge into the river, resulting in a gradual decrease in the range of the groundwater counter current.

Changes in the water exchange between surface saltwater and aquifer were also a significant contributor to saltwater intrusion caused by the influence of tidal rivers. The greatest variation in the area affected by *SWI* was estimated to be 2.14 km^2, or 5% of the total area affected by *SWI*. Ignoring such range changes will result in negatively impact coastal groundwater management. In addition, the Cl^- concentration of the groundwater discharged into the river upstream of the tidal dam was greater than 250 mg/L, indicating that saltwater in the tidal river can bypass the rubber dam and pollute the river via the aquifer.

The maximum value of *TNSE* always appeared at the falling mid-tide stage. The tide was the most influential factor in determining the *TNSE*. The *TNSE* downstream of the rubber dam was approximately 20 times greater than that upstream, indicating that rubber dams can be used to mitigate *SWI*. In addition, the tidal dam can increase the tidal river level and amplify the tide's effects on groundwater.

Understanding the impact of tidal rivers on upstream *SWI* has significant ramifications for the management of tidal rivers and coastal aquifers. This study is the beginning of an investigation into the effects of tidal rivers on the upstream groundwater flow and solute transport in coastal aquifers. Future research will investigate the effects of tide-induced variations in salinity, tidal dam, and water level of the upstream river on groundwater flow and solute transport.

Acknowledgments: This work was supported by the National Natural Science Foundation of the China-Shandong Joint Fund (No. U1806210), and National Natural Science Foundation of China (No. 42002250).

References

Ataie-Ashtiani, B., Volker, R. E., Lockington, D. A. (1999). Tidal effects on sea water intrusion in unconfined aquifers. Journal of Hydrology. 216, 17-31. https://doi.org/10.1016/S0022-1694(98)00275-3.

Cai, H., Savenije, H., Zuo, H., Jiang, C., Chua, V. (2015). A predictive model for salt intrusion in estuaries applied to the Yangtze estuary. Journal of Hydrology. 529: 1336-1349. https://doi.org/10.1016/j.jhydrol.2015.08.050.

Cheng, X., Zhan, W., Guo, Z. (2012). A modeling study on saltwater intrusion to western four watercourses in the Pearl River estuary. *China Ocean Eng* 26**,** 575–590. https://doi.org/10.1007/s13344-012-0044-y.

Fang, Y., Zheng, T., Zheng, X., Yang, H., Wang, H., Walther, M. (2021). Influence of tide-induced unstable flow on seawater intrusion and submarine groundwater discharge. Water Resources Research, 57, e2020WR029038. https://doi.org/10.1029/2020WR029038.

Gardner, L. R. (2007). Role of stratigraphy in governing pore water seepage from salt marsh sediments. Water Resources Research. 43, W07502. https://doi.org/10.1029/2006WR005338.

Gong, W., Shen, J.The response of salt intrusion to changes in river discharge and tidal mixing during the dry season in the Modaomen Estuary, China. Continental Shelf Research. 31: 769-788. https://doi.org/10.1016/j.csr.2011.01.011.

Jeong, S., Yeon, K., Hur, Y., Oh, K. (2010). Salinity intrusion characteristics analysis using EFDC model in the downstream of Geum River. Journal of Environmental Sciences. 22 (6): 934-939. https://doi.org/10.1016/S1001-0742(09)60201-1.

Kuan, W. K., Jin, G., Xin, P., Robinson, C. E., Gibbes, B., Li, L. (2012). Tidal influence on seawater intrusion in unconfined coastal aquifers. Water Resources Research, 48, 136–149. https://doi.org/10.1029/2011wr010678.

Kuan, W. K., Xin, P., Jin, G., Robinson, C. E., Gibbes, B., Li, L. (2019). Combined effect of tides and varying inland groundwater input on flow and salinity distribution in unconfined coastal aquifers. Water Resources Research. 55, 8864–8880. https://doi.org/10.1029/2018wr024492.

Lenkopane, M., Werner, A. D., Lockington, D. A., & Li, L. (2009). Influence of variable salinity conditions in a tidal creek on riparian groundwater flow and salinity dynamics. Journal of Hydrology, 375, 536–545. https://doi.org/10.1016/j.jhydrol.2009.07.004.

Li, H. L., Boufadel, M. C., Weaver, J. W. (2008). Tide-induced seawater-groundwater circulation in shallow beach aquifers. Journal of Hydrology, 352, 211–224. https://doi.org/10.1016/j.jhydrol.2008.01.013.

Lu, C., Xin, P., Li, L., Luo, J. (2015). Seawater intrusion in response to sea-level rise in a coastal aquifer with a general-head inland boundary. Journal of Hydrology. 522: 135-140. https://doi.org/10.1016/j.jhydrol.2014.12.053.

Lu, C., Shi, W., Xin, P., Wu, J., Werner, A. D. (2017). Replenishing an unconfined coastal aquifer to control seawater intrusion: injection or infiltration? Water Resources Research. 53(6): 4775-4786. https://doi.org/10.1002/2016WR019625.

Lu, C., Werner, A. D. (2013). Timescales of seawater intrusion and retreat. Advances in Water Resources, 59: 39-51. https://doi.org/10.1016/j.advwatres.2013.05.005.

Moffett, K. B., Wolf, A., Berry, J. A., and Gorelick, S. M. (2010). Salt marsh-atmosphere exchange of energy, water vapor, and carbon dioxide: effects of tidal flooding and biophysical controls. Water Resources Research. 46, W10525. doi:10.1029/2009WR009041.

Muchamad, W., Trinugroho, B. B., Muhammad, B. (2020). The seawater intrusion under dam failure in the Cimanuk River Estuary, Indonesia. Regional Studies in Marine Science. 36, 101267, https://doi.org/10.1016/j.rsma.2020.101267.

Prandle, D. (2004). How tides and river flows determine estuarine bathymetries. Progress in Oceanography. 61 (1): 1-26. https://doi.org/10.1016/j.pocean.2004.03.001.

Robinson, C., Gibbes, B., & Li, L. (2006). Driving mechanisms for groundwater flow and salt transport in a subterranean estuary. Geophysical Research Letters, 33, L03402. https://doi.org/03410.01029/02005GL025247.

Sefelnasr, A., Sherif, M. (2014). Impacts of seawater rise on seawater intrusion in the Nile Delta aquifer, Egypt. Groundwater. 52 (2), 264–276. https://doi.org/10.1111/gwat.12058.

Shen, C., Jin, G., Xin, P., Kong, J., & Li, L. (2015). Effects of salinity variations on pore water flow in salt marshes. Water Resources Research, 51, 4301–4319. https://doi.org/10.1002/2015WR016911.

Sherif, M., Sefelnasr, A., Javadi, A. (2012). Incorporating the concept of equivalent freshwater head in successive horizontal simulations of seawater intrusion in the Nile

Delta aquifer, Egypt. Journal of Hydrology. s464–465 (20), 186–198. https://doi.org/10.1016/j.jhydrol.2012.07.007.

Shi, L., Lu, C., Ye, Y., Xie, Y., WU, J. (2020). Evaluation of the performance of multiple-well hydraulic barriers on enhancing groundwater extraction in a coastal aquifer. Advances in Water Resources. 144. https://doi.org/10.1016/j.advwatres.2020.103704.

Tully, K., Gedan, K., Epanchin-Niell, R., Strong, A., Bernhardt, E.S., BenDor, T., Mitchell, M., Kominoski, J., Jordan, T.E., Neubauer, S.C., Weston, N.B. (2019). The Invisible Flood: The Chemistry, Ecology, and Social Implications of Coastal Saltwater Intrusion. BioScience. 69, 368–378. https://doi.org/10.1093/biosci/biz027.

Wang, J., Li, L., He, Z., Noor, A. K., Xu, D. (2019). Numerical modelling study of seawater intrusion in Indus River Estuary, Pakistan. Ocean Engineering. 184: 74-84, https://doi.org/10.1016/j.oceaneng.2019.05.029.

Walther, M., Delfs, J.-O., Grundmann, J., Kolditz, O., & Liedl, R. (2012). Saltwater Intrusion Modeling: Verification and Application to an Agricultural Coastal Arid Region in Oman. Journal of Computational and Applied Mathematics. http://dx.doi.org/10.1016/j.cam.2012.02.008.

Werner, A.D., Lockington, D.A., 2006. Tidal impacts on riparian salinities near estuaries. Journal of Hydrology. 328 (3–4), 511–522.

Werner, A. D., Bakker, M., Post, V. E. A., Vandenbohede, A., Lu, C., Ataie-Ashtiani, B., et al. (2013). Seawater intrusion processes, investigation and management: Recent advances and future challenges. Advances in Water Resources, 51, 3-26. https://doi.org/10.1016/j.advwatres.2012.03.004.

Wilson, A. M., Gardner, L. R. (2006). Tidally driven groundwater flow and solute exchange in a marsh: Numerical simulations. Water Resources Research. 42, W01405. https://doi.org/01410.01029/02005WR004302

Wilson, A. M., Morris, J. T. (2012). The influence of tidal forcing on groundwater flow and nutrient exchange in a salt marsh-dominated estuary. Biogeochemistry, 108(1-3), 27-38. https://doi.org/10.1007/s10533-010-9570-y.

Xiao, K., Wu, J., Li, H., Hong, Y., Wilson, A. M., Jiao, J. J., Shananan, M. (2018). Nitrogen fate in a subtropical mangrove swamp: potential association with seawater-groundwater exchange. Science of the total environment, 635, 586–597. https://doi.org/10.1016/j.scitotenv.2018.04.143.

Xiao, K., Li, H., Xia, Y., Yang, J., Wilson, A. M., Michael, H. A., et al (2019). Effects of tidally varying salinity on groundwater flow and solute transport: insights from modelling an idealized creek marsh aquifer. Water Resources Research, 55, 9656–9672. https://doi.org/10.1029/2018WR024671.

Xin, P., Robinson, C., Li, L., Barry, D. A., Bakhtyar, R. (2010). Effects of wave forcing on a subterranean estuary. Water Resources Research, 46, W12505. https://doi.org/12510.11029/12010WR009632.

Xin, P., Yuan, L. R., Li, L., Barry, D. A. (2011). Tidally driven multiscale pore water flow in a creek-marsh system. Water Resources Research, 47, W07534. https://doi.org/10.1029/2010wr010110.

Xue, P., Chen, C., Ding, P., Beardsley, R. C., Lin, H., Ge, J., and Kong, Y. (2009), Saltwater intrusion into the Changjiang River: A model-guided mechanism study, J. Geophysical. Research. 114, C02006, doi:10.1029/2008JC004831.

Yu, X., Xin, P., Lu, C. (2019). Seawater intrusion and retreat in tidally-affected unconfined aquifers: Laboratory experiments and numerical simulations. Advances in Water Resources. 132, 103393,https://doi.org/10.1016/j.advwatres.2019.103393.

Zahed, F., Etemad-Shahidi, A., Jabbari, E. (2008). Modeling of salinity intrusion under different hydrological conditions in the Arvand river estuary. Canadian Journal of Civil Engineering. https://doi.org/10.1139/L08-087.

Zou, H., Li, H. (2010). Numerical simulation of seawater intrusion from estuary into river using a coupled modeling system. Journal of Ocean University of China. 9: 219–229. https://doi.org/10.1007/s11802-010-1722-0.

Zhang, E., Hubert, Savenije H., Wu, H., Kong, Y., Zhu, J. (2011). Analytical solution for salt intrusion in the Yangtze Estuary, China. Estuarine, Coastal and Shelf Science. 91 (4): 492-501, https://doi.org/10.1016/j.ecss.2010.11.008.

Zhang B., Zheng, T., Zheng, X., Marc W. (2021). Utilization of pit lake on the cleaning process of residual saltwater in unconfinfined coastal aquifers. Science of the total environment, 770, 144670. https://doi.org/10.1016/j.scitotenv.2020.144670.

Zhang, D., Yang, Y., Wu, J., Zheng, X., Liu, G., Sun, X., Lin, J., Wu, J. (2020). Global sensitivity analysis on a numerical model of seawater intrusion and its implications for coastal aquifer management: a case study in Dagu River Basin, Jiaozhou Bay, China. Hydrogeology Journal. 28:2543–2557. https://doi.org/10.1007/s10040-020-02219-6.

Zheng, T., Zheng, X., Chang, Q., Zhan, H., Walther, M. (2020). Timescale and effectiveness of residual saltwater desalinization behind subsurface dams in an unconfined aquifer. Water resources research. e2020WR028493. https://doi.org/10.1029/2020WR028493.